Nanoscale

PAPER

View Article Online
View Journal | View Issue

Cite this: *Nanoscale*, 2015, **7**, 7896

High-quality, large-area $MoSe_2$ and $MoSe_2/Bi_2Se_3$ heterostructures on AlN(0001)/Si(111) substrates by molecular beam epitaxy†

E. Xenogiannopoulou,[a] P. Tsipas,[a] K. E. Aretouli,[a] D. Tsoutsou,[a] S. A. Giamini,[a] C. Bazioti,[b] G. P. Dimitrakopulos,[b] Ph. Komninou,[b] S. Brems,[c] C. Huyghebaert,[c] I. P. Radu[c] and A. Dimoulas*[a]

Received 20th November 2014,
Accepted 23rd March 2015

DOI: 10.1039/c4nr06874b

www.rsc.org/nanoscale

Atomically-thin, inherently 2D semiconductors offer thickness scaling of nanoelectronic devices and excellent response to light for low-power versatile applications. Using small exfoliated flakes, advanced devices and integrated circuits have already been realized, showing great potential to impact nanoelectronics. Here, high-quality single-crystal $MoSe_2$ is grown by molecular beam epitaxy on AlN(0001)/Si(111), showing the potential for scaling up growth to low-cost, large-area substrates for mass production. The $MoSe_2$ layers are epitaxially aligned with the aluminum nitride (AlN) lattice, showing a uniform, smooth surface and interfaces with no reaction or intermixing, and with sufficiently high band offsets. High-quality single-layer $MoSe_2$ is obtained, with a direct gap evidenced by angle-resolved photoemission spectroscopy and further confirmed by Raman and intense room temperature photoluminescence. The successful growth of high-quality $MoSe_2/Bi_2Se_3$ multilayers on AlN shows promise for novel devices exploiting the non-trivial topological properties of Bi_2Se_3.

Introduction

The isolation of various 2D layered transition metal dichalcogenides (TMDs) in recent years has given a large boost to research designing van der Waals 2D structures with tailored properties depending on the material and the layer thickness.[1–3] TMDs with the general chemical formula MX_2 (M = Mo, W; X = S, Se, Te) are indirect semiconductors exhibiting an indirect-to-direct band gap crossover when their thickness is reduced from a few layers to a single layer. The direct band gap in single layers results in intense room temperature photoluminescence (PL)[4] and more generally yields an excellent response to light in the visible and near-IR region of the solar spectrum, enabling a wide range of applications from optoelectronics[5–8] to energy conversion.[8] Owing to the strong covalent bonds within the MX_2 molecule, these materials exhibit high mechanical strength, and since they can be grown a few atoms thick they are stretchable and bendable, so they could be used for flexible transparent displays and a number of low-power versatile applications.[1] Furthermore, the low dielectric constant (~4) and the ability to reduce the channel to a single layer of atoms without severely degrading mobility offer excellent electrostatic control, allowing for aggressive lateral scaling beyond that presently achieved using silicon or other conventional semiconductors.

Using TMDs, mainly MoS_2, advanced field effect transistors[9–11] and generic integrated circuits (*e.g.* inverters, ring oscillators, SRAM, NOR gates)[12,13] have been demonstrated, showing this material's potential to impact nanoelectronics. So far, most of the research device work[9–12] has been performed on small (micron-sized) exfoliated flakes, while for mass production, large area synthesis of TMDs on insulating substrates is required to ensure reproducibility, high crystalline quality and homogeneity, and ease of device fabrication. Most attempts to synthesize TMDs are based on CVD-like methods used first for the growth of MoS_2[14] and then applied to $MoSe_2$ growth.[15–17] These methods produce single crystals with sizes up to a few hundred microns,[16] however, polycrystallinity, incomplete coverage and thickness uniformity are important issues.

[a]*Institute of Nanoscience and Nanotechnology, NCSR DEMOKRITOS, GR-15310 Athens, Greece. E-mail: dimoulas@ims.demokritos.gr*
[b]*Physics Department, Aristotle University of Thessaloniki, GR-54124 Thessaloniki, Greece*
[c]*Imec, Kapeldreef 75, Leuven, Belgium*

†Electronic supplementary information (ESI) available: crystal structure of $MoSe_2$; large area STM images of 3 ML $MoSe_2$/AlN; large area optical and SEM images of $MoSe_2$ films on AlN; GPA lattice strain analysis map of 3 ML $MoSe_2$ deposited on AlN; band diagram reconstruction of $MoSe_2$/AlN and $MoSe_2/Bi_2Se_3$/AlN; short-scale uniformity investigation of 1 ML $MoSe_2$ on AlN(0001); stability investigation of 1 ML $MoSe_2$ on AlN(0001); large area TEM image of $MoSe_2$ on AlN(0001). See DOI: 10.1039/c4nr06874b

Molecular beam epitaxy (MBE) of $MoSe_2$ on suitable crystalline substrates is expected to give highly-oriented single crystals over the entire wafer. Apart from early pioneering work[18] there is a very recent report on the MBE growth of atomically-thin epitaxial $MoSe_2$ on graphene-terminated 6H-SiC (0001) substrates,[19] mainly focusing on the electronic band structure by angle-resolved photoelectron spectroscopy (ARPES). There is little information about the structural quality, the band alignment and the optical emission properties of epitaxial single and few-layer $MoSe_2$ grown by MBE on alternative insulating substrates.

In this work, we demonstrate high-quality few-layer (1–6 ML) $MoSe_2$ grown epitaxially on AlN(0001)/Si(111) substrates by MBE with or without a buffer layer. We show that using AlN crystalline templates it is possible to obtain highly-oriented single crystals of single- or few-layer $MoSe_2$ over the entire wafer (up to two inches) exhibiting high quality, very good uniformity and excellent stability in air, as verified by Raman characterization and room temperature photoluminescence. We also show that very good quality $MoSe_2$ can be grown on Bi_2Se_3 and that epitaxial $MoSe_2/Bi_2Se_3$ multilayers can be produced, thus creating the prospect for novel devices to exploit the non-trivial topological insulator properties[20] of Bi_2Se_3.

Experimental

Thin film growth and structural characterization

Film growth was carried out in an UHV–MBE system with base pressure in the 10^{-10} Torr range. All growth procedures were monitored by a reflection high energy electron diffraction (RHEED) technique using a 15 keV e-gun. $MoSe_2$ was deposited either directly on 200 nm AlN/Si(111) substrates or with a thin (3 or 5 quintuples (QL)) epitaxial Bi_2Se_3 buffer layer.

The 200 nm Al-face AlN(0001) layers were epitaxially grown by MOCVD on B-doped p-type 1150 μm Si(111) substrates, with a resistivity >1 ohm cm. The AlN was unintentionally n-type doped, typical for MOCVD-grown AlN layers. The AlN substrates received both *ex situ* and *in situ* cleaning in the MBE chamber, following the procedure described in ref. 20.

High purity Mo (99.95%) and Se (99.999%) were evaporated from an electron gun evaporator and an effusion cell, respectively, under Se-rich conditions, with a Mo/Se flux ratio of ~1 : 10 and a $MoSe_2$ growth rate of 3 ML min^{-1}. Bi_2Se_3 buffer layer growth on the 200 nm AlN(0001)/Si(111) substrate was performed by evaporating Bi (99.997%) and Se (99.999%) both from effusion cells with a Bi/Se flux ratio of ~1 : 20 and a growth rate of 1.5 QL min^{-1}.

After $MoSe_2$/AlN layer deposition, the samples were transferred to the STM chamber attached to the MBE growth chamber for *in situ* STM characterization. STM topographies were obtained in UHV (base pressure of low 10^{-9} mbar) at RT using an Omicron Large Sample SPM microscope with a Pt/Ir tip.

For the HRTEM characterization, cross-section TEM specimens were prepared by the sandwich technique. Mechanical grinding followed by focused Ar^+ ion milling in the GATAN PIPS was used to thin the specimens to electron transparency. HRTEM observations were performed using a 200 kV JEOL 2011 microscope; spherical aberration coefficient C_s = 0.5 mm and point resolution 0.192 nm. Thickness-defocus HRTEM image maps were simulated using the EMS[21] software package and were associated to the HRTEM experimental images.

Physical and chemical characterization

In situ ARPES was conducted at RT in a μ-metal analytical chamber equipped with a 100 mm hemispherical electron analyzer (SPECS PHOIBOS100) and a 2D CCD detector. The energy resolution of the detection system was better than 40 meV, while the total experimental energy resolution was ~100 meV,[22,23] dominated by the thermal broadening at RT. The excitation source was a He discharge lamp (SPECS UVS35/10) with He I (He II) radiation at 21.22 eV (40.814 eV). Photoelectrons emitted by the samples were measured in the energy distribution curve (EDC) mode. *In situ* X-ray photoelectron spectroscopy (XPS) was performed with excitation by Mg K_α radiation (1253.6 eV) using a SPECS XR50 source, at a take-off angle of 52°.

For Raman spectroscopy a 532 nm laser beam was used with a power of ~2 mW on the sample surface. Spectra were resolved by a spectrometer using a grating of 1800 l mm^{-1} and acquired by an EMCCD detector. A 100× objective lens was used and the FWHM of the laser beam intensity at the sample surface was ~1 μm. For the photoluminescence (PL) spectroscopy measurements, a 100× objective lens was used in combination with a grating of 600 l mm^{-1}. Both Raman and PL measurements were performed at RT.

Electronic structure calculations

The calculations were performed within the density functional theory (DFT) framework by using the Vienna *ab initio* simulation package. The Perdew–Burke–Ernzerhof with dispersion (PBE-D) exchange–correlation functional was engaged for our calculations. Spin–orbit effects were treated self-consistently. All atoms were allowed to relax until the force and the energy had converged to 10^{-2} eV $Å^{-1}$ and 10^{-4} eV, respectively.

Results and discussion

$MoSe_2$ growth on AlN and on a Bi_2Se_3 buffer layer

$MoSe_2$ was grown using a two-step process. Initially, $MoSe_2$ was deposited on AlN/Si(111) substrates at the relatively low temperature of 350 °C, where a blurred RHEED pattern was observed, indicating poor crystalline quality. In the second step, a post-deposition annealing in UHV was performed at 690 °C. The result was that the crystallinity was substantially improved, as evidenced by the RHEED streaky pattern in Fig. 1g and h, although a slightly disordered surface may not be excluded considering that the streaks are not as sharp as in the case of the clean AlN surface (Fig. 1a and b). The streaky RHEED pattern in both [11–20] and [1–100] azimuths of a 1 ML $MoSe_2$ in Fig. 1g and h, respectively, indicates that the two hexagonal unit cells are perfectly aligned such that

$[11\text{–}20]_{MoSe_2}//[11\text{–}20]_{AlN}$ and $[1\text{–}100]_{MoSe_2}//[1\text{–}100]_{AlN}$ in the plane. It is worth noting that the RHEED beam covers an area of a few mm at least, which is a significant portion of the cm-scale wafer. The absence of additional streaks also indicates the absence of rotated 30° or 90° domains, meaning that the layers are highly-oriented single crystals extended over a large part of, if not the entire wafer. The small, almost undetectable difference in the relative positions of the streaks (Fig. 1a and g) reflects the rather small lattice mismatch of ~6% between the $MoSe_2$ and AlN (a_{AlN} = 3.11 Å, a_{MoSe_2} = 3.299 Å) at room temperature; the latter nearly-matched condition may be the reason for the perfect orientation of the $MoSe_2$ crystal relative to the substrate.

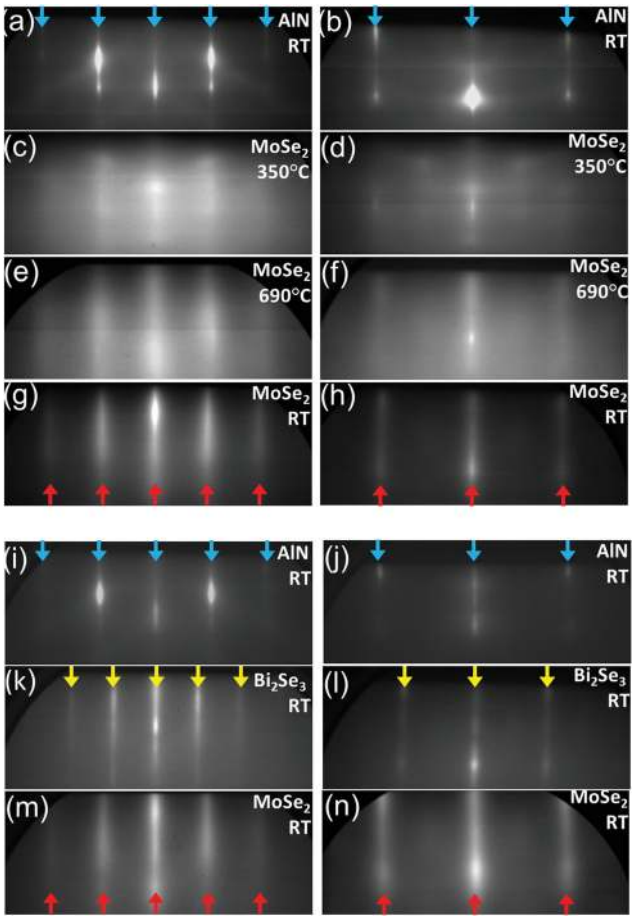

Fig. 1 RHEED patterns of: (a–h) 1 ML $MoSe_2$ deposited on AlN(0001) by the 2 step-process, and (i–n) 2 ML $MoSe_2$ deposited on a 5 QL Bi_2Se_3 buffer layer, epitaxially grown on AlN(0001). (a) and (i) show the bare AlN (0001) pattern along the [11–20] azimuth and (b and j) bare AlN(0001) along the [1–100] azimuth. (c) and (d) are recordings at 350 °C after the deposition of $MoSe_2$, (e) and (f) are recordings at 690 °C after the post-deposition annealing step, while (g) and (h) present the $MoSe_2$ film on AlN after final cooling down to RT. In (e) and (f) $MoSe_2$ becomes highly crystalline with the respective crystal orientations aligned to those of AlN, which is clearly observed after cooling down in (g) and (h). (k) and (l) show a 5 QL Bi_2Se_3 buffer layer grown epitaxially on AlN(0001) at 300 °C with high crystalline quality, (m) and (n) show that $MoSe_2$ deposited on the Bi_2Se_3 buffer layer at 300 °C grows epitaxially, with $[11\text{–}20]_{MoSe_2}//[11\text{–}20]_{Bi_2Se_3}$ and $[1\text{–}100]_{MoSe_2}//[1\text{–}100]_{Bi_2Se_3}$. The blue and yellow downward arrows show AlN and Bi_2Se_3 streaks, respectively. The red upward arrows show $MoSe_2$ streaks.

Recently, our group reported[20] the high-quality epitaxial growth of Bi_2Se_3 thin films on AlN(0001) substrates, which motivated us to use 5 quintuple layers (QL) of Bi_2Se_3 as a buffer layer for 2 ML $MoSe_2$ overgrowth. The results in Fig. 1i–n show that both Bi_2Se_3 and $MoSe_2$ layers are epitaxial and perfectly oriented with the AlN substrate, such that $[11\text{–}20]_{MoSe_2}//[11\text{–}20]_{Bi_2Se_3}//[11\text{–}20]_{AlN}$ and $[1\text{–}100]_{MoSe_2}//[1\text{–}100]_{Bi_2Se_3}//[1\text{–}100]_{AlN}$. It is remarkable that $MoSe_2$ is grown highly oriented on Bi_2Se_3 despite the large mismatch of about 20% between the two materials. The growth of $MoSe_2$ is constrained to low temperatures due to the limited thermal stability of the underlying Bi_2Se_3 buffer, which decomposes in vacuum at temperatures higher than 300 °C. Nevertheless, the presence of the Bi_2Se_3 buffer layer promotes the growth of $MoSe_2$ at much lower substrate temperatures (300 °C) compared to its direct deposition on the AlN(0001) substrate (690 °C), without reduction in epitaxial quality. The ability to reduce the growth temperature of such 2D materials could be advantageous for large-scale device manufacturing, especially for applications where heterogeneous integration with Si devices is required.

Film structural characterization

The surface structure of a 3 ML $MoSe_2$ sample was imaged *in situ* by UHV–STM, as depicted in Fig. 2. The high resolution image (Fig. 2a) shows the hexagonal symmetry of the lattice. The brighter spots in Fig. 2a represent Se atoms located in the three corners of the top hexagon (Fig. 2b)[24] separated by a distance of 3.3 Å, as shown in the line 1 scan in Fig. 2c. This is in good agreement with the theoretical value of the lattice constant a_{MoSe_2} = 3.299 Å. The Mo atoms are located in the three corners of the hexagon located 1.67 Å below the top one (see also ESI, Fig. S1a†). This picture is further supported by the line 2 scan in Fig. 2d, showing that the Mo atoms are in a lower position and have a distance of ~2 Å from neighboring Se atoms, close to the theoretical value of 1.9 Å. STM performed on a larger scale (see ESI, Fig. S2a, b†), reveals that at the low deposition temperature the sample has a root mean square (RMS) surface roughness value of 1.25 nm, which, however, significantly improves after post-deposition annealing (see ESI, Fig. S2c, d†) yielding a RMS roughness of 0.62 nm, over a scanned area of 5 × 5 μm^2. The annealed sample shows a continuous film with smooth surface morphology.

Additionally, large-area optical images of samples with different sizes and parts of the sample inspected by SEM, (see ESI, Fig. S3†) indicate a uniform, homogeneous film over the entire substrate.

The film microstructure was examined by high resolution transmission electron microscopy (HRTEM) (Fig. 3). A low-magnification cross section TEM image is presented in Fig. 3a, showing a 3 ML $MoSe_2$ film of uniform thickness and smooth surface and interface with the AlN substrate, as also verified by large area STM images (see also ESI, Fig. S2†).

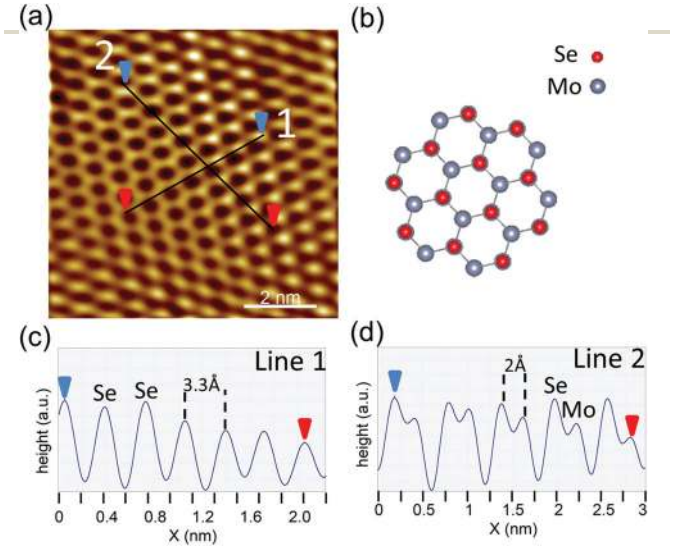

Fig. 2 (a) Room temperature high resolution STM image of 3 ML $MoSe_2$ on AlN(0001) (U_{bias} = 0.7 V, I = 0.9 nA), showing a honeycomb structure. The bright corners in the honeycomb configuration are attributed to Se atoms occupying the three corners of the topmost hexagon. (b) Stick and ball model of $MoSe_2$ honeycomb structure along the $[0001]_{MoSe_2}$ axis showing the Se and Mo atom positions. The Se atoms reside on the three corners of the top hexagon while Mo occupies the three corners of a hexagon located 1.67 Å below the top one. (c) Profile along line 1 in image (a) showing the estimated distance of 3.3 Å between Se atoms, in good agreement with the $MoSe_2$ lattice constant a_{MoSe_2} = 3.299 Å. (d) Profile along line 2 in image (a) showing the buckling between Se and Mo atoms and their estimated lateral distance of 2 Å, close to the theoretical value of 1.9 Å.

The HRTEM image of Fig. 3b shows 3 layers of $MoSe_2$ imaged along the $[11\text{–}20]_{AlN}$ zone axis. The corresponding simulated image (thickness 15 nm along the electron beam, defocus −70 nm) superimposed on the right side confirms that the [11–20] directions of the AlN and $MoSe_2$ lattices are aligned in agreement with the RHEED data in Fig. 1. The intense bright rows correspond to the space between the $MoSe_2$ layers (Se atoms appear dark), whilst Mo atoms are represented by the bright dotted rows in between (see also ESI, Fig. S1b†). Fig. 3c shows the same sample imaged along the $[1\text{–}100]_{AlN}$ zone axis. Similarly, the dark rows correspond to the $MoSe_2$ layers and bright areas to the space between them. Because of the dense atom configuration along this direction (see also ESI, Fig. S1c†), no atoms are resolved in the dark areas in contrast to Fig. 3b. Fig. 3d and 3e show 2 ML of $MoSe_2$ grown on top of 5 QL epitaxial Bi_2Se_3 buffer, and 2 ML of $MoSe_2$ sandwiched between two Bi_2Se_3 layers, each 3 QL thick, respectively. The corresponding image simulation is shown as an inset in Fig. 3e (thickness 8.5 nm, defocus −70 nm), in which the bright dotted rows correspond to Mo atoms. In summary, the data in Fig. 3 (combined with the RHEED data) show that high-quality epitaxial $MoSe_2$ and $MoSe_2/Bi_2Se_3$ multilayers can be grown on AlN substrates with flat surface morphology and clean, crystalline interfaces.

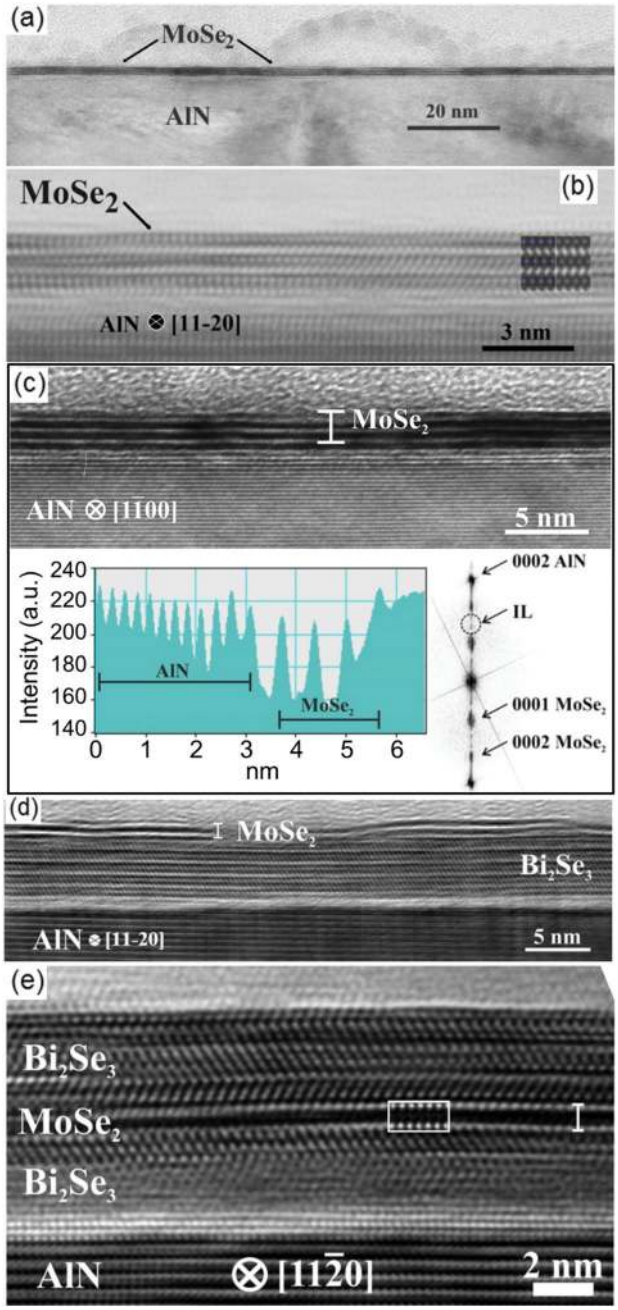

Fig. 3 (a–c) Cross section HRTEM images of 3 ML $MoSe_2$ grown on AlN (0001), viewed in low magnification (a) along $[11\text{–}20]_{AlN}$, with the corresponding simulated image as an inset in (b), and along $[1\text{–}100]_{AlN}$ in (c). In (b) and (c), $MoSe_2$ is located in the darker contrast areas, while the very bright rows, more pronounced in (c), show the separation between the $MoSe_2$ layers. In (c) a crystalline $MoSe_2$/AlN interface is shown with the corresponding absorption contrast profile (left side) showing lattice fringes. The fringe spacing of the top three AlN layers increases gradually. The Fast Fourier Transform (FFT) (right side), calculated from the HRTEM image, is presented showing the points that represent the spatial frequencies contained. (d) HRTEM images of 2 ML $MoSe_2$ deposited on a 5 QL Bi_2Se_3 buffer layer grown on AlN(0001), viewed along $[11\text{–}20]_{AlN}$. (e) 3 QL Bi_2Se_3/2 ML $MoSe_2$/3QL Bi_2Se_3 heterostructure deposited on AlN(0001) at 300 °C, viewed along $[11\text{–}20]_{AlN}$ (inset, the corresponding $MoSe_2$ simulated image). (b–e) show that $MoSe_2$ grows epitaxially with high crystalline quality on both AlN and the Bi_2Se_3 buffer layer on AlN. The $MoSe_2$ films grown on AlN show a smooth surface and interface morphology.

A small distortion of AlN just underneath $MoSe_2$ can be seen in Fig. 3b and 3c. The appearance of an interlayer in the TEM pictures could be attributed to an artifact. Ion milling certainly affects this interface preferentially, given the weakness of the van der Waals bonding and the fact that AlN is easily amorphized under the ion beam. In this regard, some interfacial damage is expected during sample preparation. The brighter contrast of the AlN lattice fringes at the interface could be attributed to the locally smaller thickness of the foil due to the preferential thinning mentioned above. Therefore, the interfacial region is not amorphous in the as-grown sample and any amorphization is induced by the ion milling during TEM specimen preparation.

On closer examination of the interface, we have undertaken detailed measurements of the lattice fringe spacings from the cross-sectional HRTEM images[25] in Fig. 3c. Our measurements, supported by the absorption contrast profile, showed a gradual increase in the (0002) *d* spacing between the top 3 or 4 AlN lattice fringes, as shown in Fig. 3c. Furthermore, a strain mapping performed using geometrical phase analysis (GPA)[26] (see also ESI, Fig. S4†), showed an increase of up to 20% in the spacing of these fringes. The local increase of the lattice constant could be attributed either to a change in chemical composition, or to elastic strain, or to both. Elastic strain, if present, could even promote the local amorphization of these top layers under ion beam milling. A possible cause for the increase of the *d* spacing is the modification of the top 3–4 AlN layers through the incorporation of molybdenum atoms. Mo has a higher electron affinity than Al, and a larger atomic radius. The absorption contrast profile in Fig. 3c shows an increase of the lattice parameter by up to ~20% prior to the $MoSe_2$ film. Hexagonal molybdenum nitride has a 13% larger lattice constant than AlN along the growth direction,[27] so we anticipate that some elastic strain is also present. The possible reaction between $MoSe_2$ and AlN at the interface is further studied by X-ray photoelectron spectroscopy below.

Interface and band alignment characterization by XPS

In situ X-ray photoelectron spectroscopy was applied to both $MoSe_2$/AlN and $MoSe_2/Bi_2Se_3$/AlN heterostructures. The binding energies of the Mo $3d_{5/2}$ and Se $3d_{5/2}$ core levels for 1 ML $MoSe_2$ deposited directly on AlN(0001) (Fig. 4a and b) are 228.89 eV and 54.51 eV, respectively. These values are in good agreement with others reported[18] on thin-film and bulk single-crystal $MoSe_2$. The core level peak positions and line shapes indicate that only Mo–Se bonds exist. Therefore, within the detection limit of our XPS it can be inferred that $MoSe_2$ does not react with the AlN substrate in large quantities. A limited incorporation of Mo in the top 3 layers of AlN may not be excluded though, taking into consideration the HRTEM analysis of the image in Fig. 3c, as described in the previous section. Similarly, in the case of 1 ML $MoSe_2$ deposited on a 3 QL Bi_2Se_3 buffer layer on AlN at 300 °C (Fig. 4c and d), the Mo $3d_{5/2}$ peak position at 229.12 eV indicates Mo–Se bonds and agrees well with $MoSe_2$ formation, while the Se 3d peak is attributed to two contributions, one to Se–Mo bonds and one to Se–Bi bonds. The Bi $4f_{7/2}$ core level binding energy of 158.52 eV (not shown here) indicates that Bi is bonded only with Se and no reaction at the Bi_2Se_3/AlN interface occurs. In addition, using tabulated sensitivity factors the Se/Mo ratios are found to be in the range of (1.9–2.05), indicating that the layers have stoichiometry close to the ideal, that is Se/Mo = 2/1.

The band offsets of the $MoSe_2$/AlN and $MoSe_2/Bi_2Se_3$/AlN heterojunctions were derived from XPS measurements (Fig. 4e

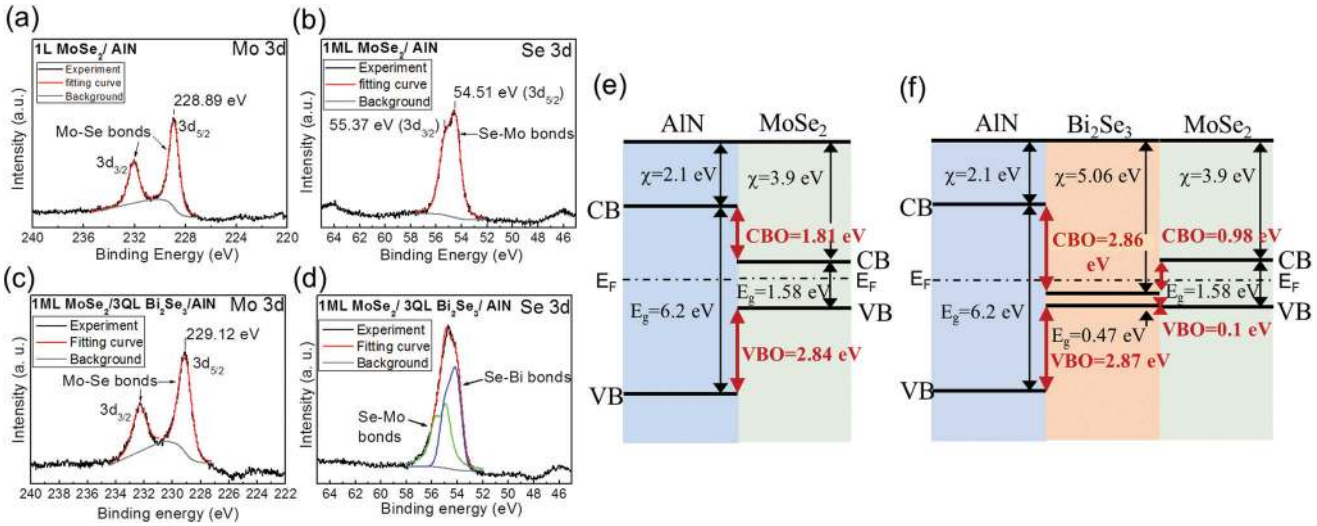

Fig. 4 (a and b) Mo 3d and Se 3d core level XPS peaks of 1 ML $MoSe_2$ grown on AlN. No reaction with the substrate is observed and the positions and line shapes of the Mo 3d and Se 3d peaks indicate Mo–Se bonding. (c and d) Mo 3d and Se 3d core level XPS peaks of 1 ML $MoSe_2$ deposited on a 3QL Bi_2Se_3 buffer layer on AlN. The Se 3d peak is attributed to Se–Mo and Se–Bi bonding, while the Mo 3d peaks indicate Mo–Se bonding. (e and f) Schematic of the $MoSe_2$/AlN and $MoSe_2/Bi_2Se_3$/AlN band offsets, as determined by XPS core level analysis. χ and E_F denote the electron affinity and the Fermi energy, respectively. E_g is the energy gap, while CBO and VBO denote the conduction and valence band offsets, respectively.

and f). In particular, the valence band offsets (VBO) were determined using Kraut's method[28] to be 2.84 eV and 2.87 eV/0.1 eV for the $MoSe_2$/AlN and Bi_2Se_3/AlN systems, respectively (see also ESI†). Accordingly, the conduction band offsets (CBO) were calculated to be 1.81 eV and 2.86 eV/0.98 eV for the $MoSe_2$/AlN and Bi_2Se_3/AlN systems, respectively, using band gap values (see also ESI†) taken from the literature. The estimated CBO and VBO between the $MoSe_2$ and AlN indicate a sufficiently high transport barrier for both electrons and holes perpendicular to the layers, implying that the AlN layer could provide sufficient insulation for the operation of $MoSe_2$-based electronic devices with minimum leakage through the substrate. It is worth noting that the XPS-reconstructed band alignments are consistent with electron affinity values, χ (see Fig. 4e and f) reported in the literature for AlN, $MoSe_2$ and Bi_2Se_3 materials[29–31] and the position of the Fermi level, E_F, with respect to the CB and VB of the layers in the stack, suggesting that there is no band bending or charge transfer at the interfaces.

Electronic band structure of $MoSe_2$ films

Fig. 5 shows the valence band structure of 1–6 ML $MoSe_2$ films grown on AlN(0001) substrates, as imaged by ARPES in the *ΓKHA* plane of the 1st BZ of $MoSe_2$,[22,32] using He I (21.22 eV) and He II (40.814 eV) excitation energies. Except for the spin splitting of the band near *K*, which is not resolved because of limited resolution (~110 meV) at room temperature, in the monolayer limit, the observed band dispersion along *Γ*–*K* (Fig. 5a and d) agrees quite well with the theoretical calculations (Fig. 5g). The valence band maximum (VBM) is located at the *K* point with a binding energy E_B = 1 eV, about (150–200) meV higher in energy than at the *Γ* point. Comparison with first principles calculations (Fig. 5g), which predict a conduction band minimum (CBM) also at the *K* point, indicates that our nominal single-layer $MoSe_2$ films have a direct band gap.[19,33,34] As the thickness increases to 3 ML (Fig. 5b and e) and 6 ML (Fig. 5c and f), the VBM switches to the *Γ*/*A* point, due to a shift of the topmost valence band to a lower binding energy (closer to E_F) around the *Γ*/*A* point, while its position at the *K*/*H* point remains at the same level. Thus, in thicker films the VBM is located at the *Γ*/*A* point (Fig. 5e and f), resulting in an indirect band gap, as predicted[33] in bulk TMDs or observed[19] in 8 ML-thick $MoSe_2$ films. The thickness dependence of the VBM around the *Γ*/*A* point is clearer in the He II data (Fig. 5 d–f).

The small difference between the He I and He II data is due to a weak dispersion $E(\vec{k}_\perp)$ around the zone center,[22,32] which is picked up by the different photon excitation energies. As thickness increases, mainly Mo $4d_{z^2}$ orbitals[22,23,32–34] contribute to the VBM around the *Γ* point through the van der Waals–interlayer interaction,[33] showing its bulk character. On the other hand the topmost VB around the *K* point shows negligible thickness dependence due to the Mo $4d_{xy/x^2-y^2}$ origin.[22,23,32–34] The data in Fig. 5 present well resolved spectra, characteristic of energy dispersion along the *ΓK* crystallographic direction in *k*-space, in agreement with theory.

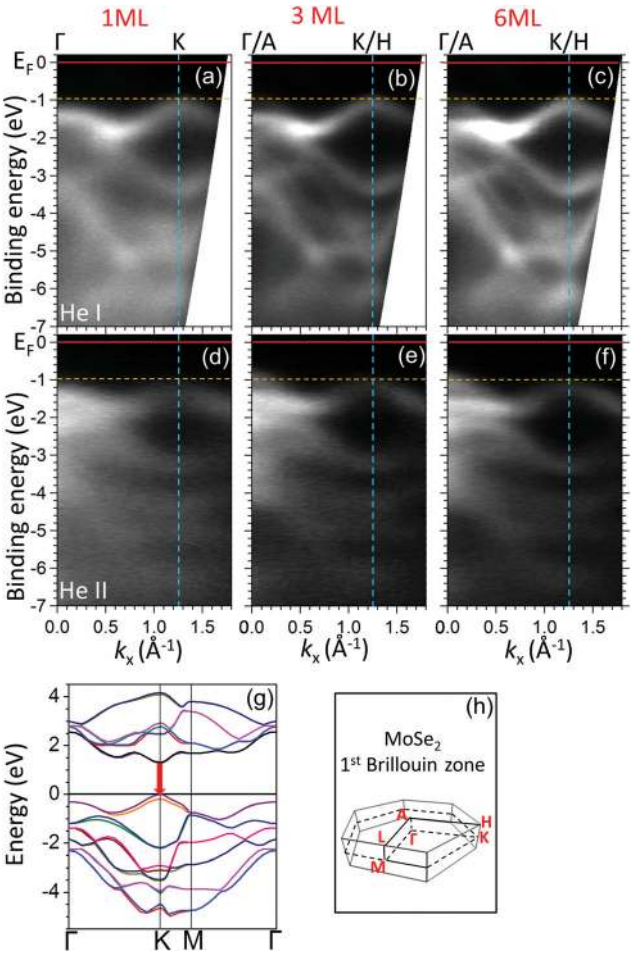

Fig. 5 Valence band structure imaging by ARPES of (1–6 ML) $MoSe_2$ layers grown on AlN(0001) substrates along the *Γ*/*A*–*K*/*H* direction of the 1st BZ of $MoSe_2$. Measurements made at RT, using (a–c) He I (21.22 eV) and (d–f) He II (40.814 eV) resonance radiation. The images in (a–f) show the binding energy as a function of the wavevector component $k_{||,x}$ parallel to the surface. In the monolayer limit (a and d) the VBM is located at the *K* point at E_B = 1 eV, indicating a direct band gap. In thicker films, at 3 ML (b and e) and 6 ML (c and f), the VBM is located at the *Γ* point, consistent with an indirect band gap. Among He I and He II data for 3 ML (b and e) and 6 ML (c and f) films, small differences in the band structure around the *Γ* point are observed. This is attributed to a small $E\left(\vec{k}_\perp\right)$ dispersion around the *Γ* point. Red solid lines indicate the E_F level position, while orange dashed lines indicate the position of the VBM at the *K*/*A* point. (g) First principles-calculated band structure of 1 ML. The red arrow indicates the direct band gap position. (h) The first Brillouin zone of the 2H structure of $MoSe_2$.

This supports our claim made on the basis of RHEED in Fig. 1 that the films are highly-oriented, essentially forming a single crystal. If several orientation domains existed, then a more complex and fuzzy dispersion would have been observed in Fig. 5, characteristic of a mixture of dispersions along different crystallographic orientations, which is not the case here.

Film quality and thickness uniformity by Raman and PL

The vibrational modes of the prepared monolayer $MoSe_2$ film on 200 nm AlN(0001)/Si(111) were investigated by Raman spec-

troscopy. The group theory analysis for bulk TMDs that are members of D_{6h} point group symmetry[35] predicts four Raman-active and two Raman-inactive modes. From the active modes, only the in-plane mode E^1_{2g} and the out-of-plane mode A_{1g} are accessible under the experimental conditions. Additionally, one Raman mode that is inactive in bulk crystals becomes optically active when the number of layers decreases, due to the breakdown of translational symmetry.[15,35] This is an interlayer vibrational mode B^1_{2g}, characterized as a breathing mode, and is present only in few-layer material and absent in a single-layer $MoSe_2$.

The typical Raman spectrum of single-layer $MoSe_2$ on AlN shown in Fig. 6a has two intense sharp Raman peaks. One is attributed to the $MoSe_2$ out-of-plane vibrational mode A_{1g} at 240.8 cm^{-1}, and one to the crystalline Si[35] substrate at 521 cm^{-1}. The in-plane E^1_{2g} mode of $MoSe_2$ is located at 288.5 cm^{-1} (clearly shown in the expanded Raman spectrum in the region of 200–400 cm^{-1} in Fig. 6d). There is no evidence of the breathing mode B_{2g} peak around 352 cm^{-1}, an area of the spectrum that is dominated by weak background signals. The bands centered at 303 cm^{-1} and 960 cm^{-1} (Fig. 6a) are associated with the 2TA and 2TO modes of crystalline Si.[36]

From the peak positions of the Raman shifts and their intensities it is difficult to distinguish between monolayer and bilayer $MoSe_2$. However, most of the evidence in this work is in favor of monolayer $MoSe_2$, and this is in good agreement with published data of monolayer $MoSe_2$ either transferred[35,37] or grown[15,17,38] on SiO_2/Si substrates. The intensity ratio between the out-of-plane A_{1g} and in-plane E^1_{2g} modes (A_{1g}/E^1_{2g}) is found to be ~23, in agreement with published values for exfoliated single-layer $MoSe_2$.[37,39] In addition, the weak or totally absent breathing mode (Fig. 6d) points to a single-layer $MoSe_2$ material.

Photoluminescence spectroscopy was used to investigate the optical emission properties of monolayer $MoSe_2$ grown on AlN, with the main aim to probe the quality of the layer and verify that the material has a direct band gap, as indicated by *in situ* ARPES. The epitaxally-grown single-layer $MoSe_2$ on AlN presents strong PL emission at room temperature, as shown in Fig. 6b, with a dominant peak at 1.55 eV and a weaker peak at 1.75 eV, attributed to direct excitonic transitions A and B, respectively, corresponding to the transitions schematically shown in Fig. 6c. Due to loss of inversion symmetry in monolayer $MoSe_2$, the VB degeneracy is lifted[19,40] under the influence of a strong spin–orbit interaction, resulting in the VB splitting near the *K* point, as predicted by DFT (Fig. 6c) and probed by PL (Fig. 6b). The measured energy difference of ~200 meV between the two PL signals agrees very well with the calculated spin–orbit splitting of ~190 meV in Fig. 6c, as well as with published experimental[15] and theoretical values.[40] The strong PL signal in Fig. 6b indicates a direct gap material, in accordance with the nominally 1 ML thickness of the grown $MoSe_2$, although the possibility of obtaining similar double-peak PL at the same energy from a bilayer $MoSe_2$ cannot be excluded.

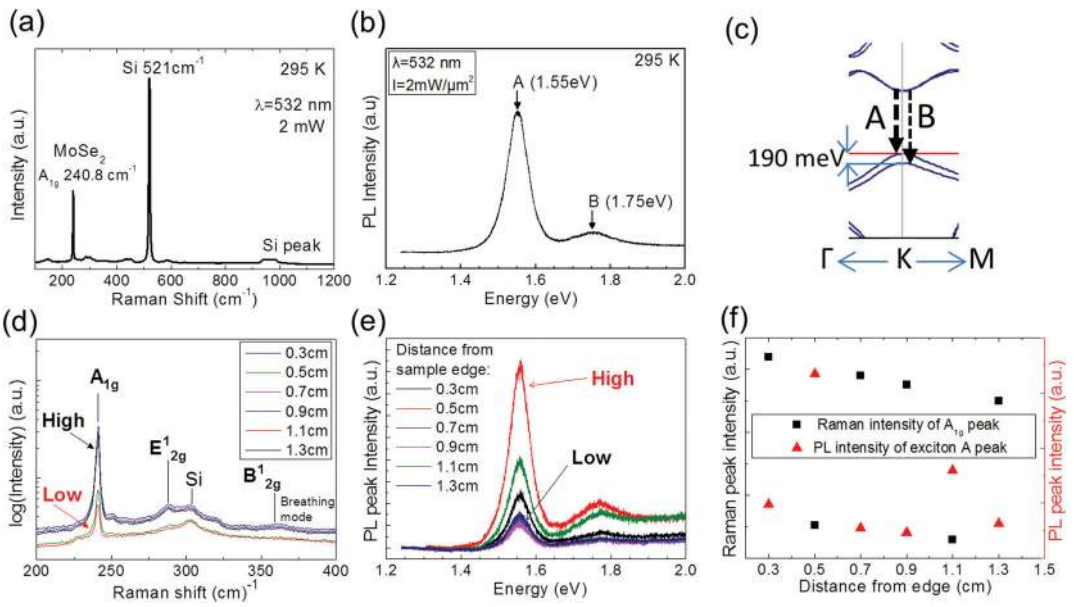

Fig. 6 (a–c) Characterization of nominally single-layer $MoSe_2$ on AlN(0001): (a) Raman spectrum showing the A_{1g} peak at 240.8 cm^{-1} associated with $MoSe_2$; (b) photoluminescence spectrum showing the presence of two excitonic peaks at 1.55 eV and 1.75 eV; (c) schematic detail of the theoretical band structure around the *K* point of 1 ML $MoSe_2$, indicating the two excitonic transitions A and B with a 190 meV energy difference due to spin–orbit splitting. The theoretically predicted energy difference is in good agreement with the measured PL peaks energy difference in (b). (d–f) Large scale uniformity investigation of a 2 × 2 cm^2 sample of the same $MoSe_2$ sample on AlN(0001): (d) Raman spectra and (e) photoluminescence spectra measured at variable distances from the sample edge; (f) correlation of Raman and PL peak intensities measured at variable distances from the sample edge. On a large scale two different behaviors are observed: the high Raman signal of the A_{1g} peak is correlated to the low PL intensity of exciton A and *vice versa*.

To extract information about uniformity in terms of structural and optical properties, the sample was probed over the entire 2 cm square substrate. On a short scale, in an area of 40 × 40 μm^2, a highly uniform layer in terms of Raman A_{1g} peak intensity, width and position was revealed (see also ESI, Fig. S5†). In general, Raman selection rules do not exclude a dependence of the Raman peak intensities on the crystal orientation, which should be reflected in the polarization of the scattered light. However, the Raman experimental set-up used here does not have an analyzer, so the detection system lacks sensitivity with respect to the polarization of the scattered radiation from the sample. Therefore, the peak intensities do not depend on the crystal orientation, as verified by arbitrarily rotating the sample (not shown here). Given the insensitivity of the different Raman peaks to crystal orientation, the intensity ratio between A_{1g} and $E^1{}_{2g}$ is an appropriate parameter for an accurate uniformity assessment of the $MoSe_2$ film. Since the $E^1{}_{2g}$ peak is small and overlaps with a nearby Si peak, both peaks are fitted simultaneously and the height of the $E^1{}_{2g}$ peak is extracted. An example of a $E^1{}_{2g}$ fitting result is given in Fig. S5.† It is clear that the $A_{1g}/E^1{}_{2g}$ Raman mapping (see also ESI, Fig. S5†) indicates a uniform $MoSe_2$ layer over a 40 × 40 μm^2 area, with an average $A_{1g}/E^1{}_{2g}$ ratio value of ~23, indicative of monolayer $MoSe_2$.[37]

On a larger scale, the sample was probed along a line that runs across the substrate from one edge to the other with 200 μm steps, and the results are summarized in Fig. 6d and e. Although the sample is very uniform over large areas, the data show a remarkable "digital" behavior mainly revealed in the Raman spectra (Fig. 6d). The Raman A_{1g} mode acquires either low or high values but no values in between. The PL (Fig. 6e) follows a similar behavior although with a larger dispersion in intensity. However, correlation with the Raman peak is observed: the PL intensity is high where the Raman intensity of A_{1g} is low and *vice versa* (Fig. 6f), a behavior that is not fully understood. Based on previous PL work on MoS_2,[4,41] it is tempting to associate the low Raman/high PL behavior with the presence of single-layer $MoSe_2$ areas and the high Raman/low PL behavior with bilayer $MoSe_2$ in other areas on the same wafer. This has to be treated with caution though, given that an abnormally high PL at room temperature has been reported[37] in few-layer $MoSe_2$. Finally, it is worth noting that uncapped single and bilayer $MoSe_2$ have been examined by Raman and PL over a period of time and they have been found to be very stable over at least two weeks while exposed to air (see also ESI, Fig. S6†).

Critical assessment of microstructure and uniformity

The characterization of large-area $MoSe_2$ films is very challenging because most of the techniques that are sensitive to microstructure such as HRTEM are sampling techniques probing only a limited area of the order of 80–100 nm in length. On such a length scale, the single crystal quality and thickness uniformity is unambiguously confirmed (Fig. 3) in several sampled areas on the wafer. Low magnification TEM can provide information about thickness uniformity on the few hundred nm scale, as for example the TEM image in Fig. S7 (ESI†), which shows a very good thickness uniformity of $MoSe_2$ over a region that exceeds 250 nm in length. Other techniques such as STM or SEM probe larger areas on the few tens of a micron or mm scales, and by using these techniques (see also ESI, Fig. S2 and S3†) we conclude that the films are continuous with full coverage over the entire 2 inch diagonal substrate, and that there are no major thickness variations across the wafer. However, these techniques are less sensitive to thickness variations at the level of a single atomic layer and to the existence of microstructures such as grains.

Orientational grain boundaries (GB) retain a crystalline structure and may be of high or low angle. In this case, the pertinent high angle GBs are the orientation twins that have not been identified in our films by RHEED, as already discussed above in connection to Fig. 1. The cross-sectional HRTEM observations are also consistent, *i.e.* no twin boundaries were observed.

Regarding low-angle GBs, plan view TEM observations are required. The preparation of such TEM specimens is difficult due to the AlN substrate, which renders useless the currently available approaches. Although it was not possible to account for such GBs from plan view TEM, we argue that if they are present to any significant extent, such GBs would consist of dislocations parallel to the growth direction. In our cross-sectional observations we did not observe any appreciable density of such defects.

The characterization and uniformity assessment of ultrathin (a few ML) $MoSe_2$ films remain big challenges. In fact, most of the techniques, including XRD, are not sensitive when applied to atomic-scale materials. Raman is a technique that has sufficient sensitivity for single-layer crystals and is extensively used for graphene and 2D MX_2-type semiconductors. This provides a rough estimate about thickness and physical properties with micron resolution probing uniformity over a 10–100 μm scale at least. The $MoSe_2$ films mapped by Raman over such a range were found to have excellent uniformity, while the same tests repeated in several parts of the wafer yielded similar excellent uniformity results.

In summary, despite the difficulties in the characterization of ultrathin films on a large area of the substrate, our investigation using a variety of techniques provides evidence that the films are continuous, covering the entire substrate, and that they do not have gross non-uniformities with respect to the thickness and the surface roughness. Moreover, electron diffraction (RHEED) and HRTEM show no evidence for randomly-oriented grains or for high- (twin) or low-angle orientational grains suggesting highly-oriented single-crystal films, epitaxially grown on cm-scale AlN substrates.

Conclusions

Here, we demonstrate the molecular beam epitaxial growth of large-area, highly-oriented single crystals of controllable single- to few-layer $MoSe_2$ films on AlN(0001)/Si substrates.

We show by HRTEM that $MoSe_2$ films on AlN(0001) have high structural quality and surface and interface morphology, confirmed also by XPS data showing stoichiometric $MoSe_2$ with no reaction at the interface with AlN. In addition, very good uniformity and excellent stability in air is evidenced by room temperature Raman and photoluminescence. We also show that $MoSe_2$ can grow with very good quality on Bi_2Se_3 buffer layers and that epitaxial $Bi_2Se_3/MoSe_2$ multilayers can be produced. As a final remark, the important role of the substrate is emphasized here. Since AlN is a wide band gap material, it offers the benefits of the $MoSe_2$ semiconductor-on-insulator integration scheme, creating the prospect for low leakage through the substrate and improved electrostatic control. This is further supported by XPS analysis, which indicates sufficiently high CBO and VBO acting as barriers for charge transport through the substrate. Moreover, AlN/Si(111) large-area (200 mm and 300 mm) wafers are readily available as they have been developed for several years in the context of III-nitride power and lighting devices. Once high quality epitaxial $MoSe_2$ is prepared on 300 mm AlN/Si wafers, devices and circuits can be realized on the same wafers, or the $MoSe_2$ layer can be transferred onto other optimal large-area substrates of choice, including flexible or transparent substrates for further device processing. Therefore AlN/Si creates the prospect for low-cost wafer-scale manufacturing of $MoSe_2$-based devices and circuits when TMD technology becomes mature enough for volume production.

Acknowledgements

The work is supported by the ERC Advanced Grant SMART-GATE-291260 and the National program of excellence (ARISTEIA-745) through the project TOP-ELECTRONICS.

Notes and references

1 Q. H. Wang, K. Kalantar-Zadeh, A. Kis, J. N. Coleman and M. S. Strano, *Nat. Nanotechnol.*, 2012, **7**, 699–711.
2 M. Xu, T. Lian, M. Shi and H. Chen, *Chem. Rev.*, 2013, **113**, 3766–3798.
3 A. K. Geim and I. V. Grigorieva, *Nature*, 2013, **499**, 419–425.
4 K. F. Mak, C. Lee, J. Hone, J. Shan and T. F. Heinz, *Phys. Rev. Lett.*, 2010, **105**, 136805.
5 H. S. Lee, S. W. Min, Y. G. Chang, M. K. Park, T. Nam, H. Kim, J. H. Kim, S. Ryu and S. Im, *Nano Lett.*, 2012, **12**, 446–701.
6 H. Fang, C. Battaglia, C. Carraro, S. Nemsak, B. Ozdol, J. S. Kang, H. A. Bechtel, S. B. Desai, F. Kronast, A. A. Unal, G. Conti, C. Conlon, G. K. Palsson, M. C. Martin, A. M. Minor, C. S. Fadley, E. Yablonovich, R. Maboudian and A. Javey, *Proc. Natl. Acad. Sci. U. S. A.*, 2014, **111**, 6198–6202.
7 J. S. Ross, P. Klement, A. M. Jones, N. J. Ghimire, Y. Yan, D. G. Mandrus, T. Taniguchi, K. Watanabe, K. Kitamura, W. Yao, D. H. Cobden and X. Xu, *Nat. Nanotechnol.*, 2014, **9**, 268–272.
8 A. Pospischil, M. M. Furchi and T. Mueller, *Nat. Nanotechnol.*, 2014, **9**, 257–261.
9 B. Radisavljevic, A. Radenovic, J. Brivio, V. Giacometti and A. Kis, *Nat. Nanotechnol.*, 2011, **6**, 147–150.
10 H. Liu, A. T. Neal and P. D. Ye, *ACS Nano*, 2012, **6**, 8563–8569.
11 H. Liu and P. D. Ye, *IEEE Electron Device Lett.*, 2012, **33**(4), 546–548.
12 B. Radisavljevic, M. B. Whitwick and A. Kis, *ACS Nano*, 2011, **5**, 9934–9938.
13 H. Wang, L. Yu, Y. H. Lee, Y. Shi, A. Hsu, M. L. Chin, L. J. Li, M. Dubey, J. Kong and T. Palacios, *Nano Lett.*, 2012, **12**, 4674–4680.
14 Y-H Lee, X. Q. Zhang, W. Zhang, M. T. Chang, C. T. Lin, K. D. Chang, Y. C. Yu, J. T. W. Wang, C. S. Chang, L. J. Li and T. W. Lin, *Adv. Mater.*, 2012, **24**, 2320–2325.
15 X. Lu, J. Lin, M. I. B. Utama, X. Gong, J. Zhang, Y. Zhao, S. T. Pantelides, J. Wang, Z. Dong, Z. Liu, W. Zhou and Q. Xiong, *Nano Lett.*, 2014, **14**, 2419–2425.
16 X. Wang, Y. Gong, G. Shi, W. L. Chow, K. Keyshar, G. Ye, R. Vajtai, J. Lou, Z. Liu, E. Ringe, B. K. Tay and P. M. Ajayan, *ACS Nano*, 2014, **8**, 5125–5131.
17 J. C. Shaw, H. Zhou, Y. Chen, N. O. Weiss, Y. Liu, Y. Huang and X. Duan, *Nano Res.*, 2014, **7**, 1–7.
18 F. S. Ohuchi, B. A. Parkinson, K. Ueno and A. Koma, *J. Appl. Phys.*, 1990, **68**, 2168–2175.
19 Y. Zhang, T. R. Chang, B. Zhou, Y. T. Cui, H. Yan, Z. Liu, F. Schmitt, J. Lee, R. Moore, Y. Chen, H. Lin, H. T. Jeng, S. K. Mo, Z. Hussain, A. Bansil and Z. X. Shen, *Nat. Nanotechnol.*, 2014, **9**, 111–115.
20 P. Tsipas, E. Xenogiannopoulou, S. Kassavetis, D. Tsoutsou, E. Golias, C. Bazioti, G. P. Dimitrakopulos, P. Komninou, H. Liang, M. Caymax and A. Dimoulas, *ACS Nano*, 2014, **8**, 6614–6619.
21 P. A. Stadelmann, *Ultramicroscopy*, 1987, **21**, 131–145.
22 R. Coehoorn, C. Haas, J. Dijkstra, C. J. F. Flipse, R. A. de Groot and A. Wold, *Phys. Rev. B*, 1987, **35**, 6195–6202.
23 S. K. Mahatha, K. D. Patel and K. S. R. Menon, *J. Phys.: Condens. Matter*, 2012, **24**, 475504.
24 K. Momma and F. Izumi, *J. Appl. Crystallogr.*, 2011, **44**, 1272–1276.
25 D. Gerthsen, E. Hahn, B. Neubauer, V. Potin, A. Rosenauer and M. Schowalter, *Phys. Status Solidi C*, 2003, (6), 1668–1683.
26 M. J. Hÿtch, F. Houdellier, F. Hüe and E. Snoeck, *Nature*, 2008, **453**, 1086–1089.
27 A. Bezinge, K. Yvon, J. Muller, W. Lengaeur and P. Ettmayer, *Solid State Commun.*, 1987, **63**, 141.
28 E. Kraut, R. Grant, J. Waldrop and S. Kowalczyk, *Phys. Rev. Lett.*, 1980, **44**, 1620.
29 C. I. Wu, A. Kahn, E. S. Hellman and D. N. E. Buchanan, *Appl. Phys. Lett.*, 1998, **73**, 1346–1348.
30 C. Gong, H. Zhang, W. Wang, L. Colombo, R. M. Wallace and K. Cho, *Appl. Phys. Lett.*, 2013, **103**, 053513.

31 J. Suh, D. Fu, X. Liu, J. K. Furdyna, K. M. Yu, W. Walukiewicz and J. Wu, *Phys. Rev. B: Condens. Matter Mater. Phys.*, 2014, **89**, 115307.
32 T. Böker, R. Severin, A. Müller, C. Janowitz, R. Manzke, D. Voss, P. Krüger, A. Mazur and J. Pollman, *Phys. Rev. B: Condens. Matter*, 2001, **64**, 235305.
33 W. S. Yun, S. W. Han, S. C. Hong, I. G. Kim and J. D. Lee, *Phys. Rev. B: Condens. Matter Mater. Phys.*, 2012, **85**, 033305.
34 S. Horzum, H. Sahin, S. Cahangirov, P. Cudazzo, A. Rubio, T. Serin and F. M. Peeters, *Phys. Rev. B: Condens. Matter Mater. Phys.*, 2013, **87**, 125415.
35 P. Tonndorf, R. Schmidt, P. Böttger, X. Zhang, J. Börner, A. Liebig, M. Albrecht, C. Kloc, O. Gordan, D. R. T. Zahn, S. Michaelis de Vasconcellos and R. Bratschitsch, *Opt. Express*, 2013, **21**, 4908.
36 T. A. Harriman, D. A. Lucca, J. K. Lee, M. J. Klopfstein, K. Herrmann and M. Nastasi, *Nucl. Instrum. Methods Phys. Res., Sect. B*, 2009, **267**, 1232–1234.
37 S. Tongay, J. Zhou, C. Ataca, K. Lo, T. S. Matthews, J. Li, J. C. Grossman and J. Wu, *Nano Lett.*, 2012, **12**, 5576–5580.
38 J. Mann, Q. Ma, P. M. Odenthal, M. Isarraraz, D. Le, E. Preciado, D. Barroso, K. Yamaguchi, G. von Son Palacio, A. Nguyen, T. Tran, M. Wurch, A. Nguyen, V. Klee, S. Bobek, D. Sun, T. F. Heinz, T. S. Rahman, R. Kawakami and L. Bartels, *Adv. Mater.*, 2014, **26**, 1399–1404.
39 N. Kumar, Q. Cui, F. Ceballos, D. He, Y. Wang and H. Zhao, *Nanoscale*, 2014, **6**, 4915–4919.
40 Z. Y. Zhu, Y. C. Cheng and U. Schwingenschlögl, *Phys. Rev. B: Condens. Matter Mater. Phys.*, 2011, **84**, 153402.
41 A. Splendiani, L. Sun, Y. Zhang, T. Li, J. Kim, C. Y. Chim, G. Galli and F. Wang, *Nano Lett.*, 2010, **10**, 1271–1275.